Biosensors and Bioelectronics 126 (2019) 143–150

Contents lists available at ScienceDirect

Biosensors and Bioelectronics

journal homepage: www.elsevier.com/locate/bios

Label-free aptasensor for the detection of cardiac biomarker myoglobin based on gold nanoparticles decorated boron nitride nanosheets

Muhammad Adeel[a], Md. Mahbubur Rahman[b,*], Jae-Joon Lee[a,*]

[a] Department of Energy Materials and Engineering, Research Center for Photoenergy Harvesting & Conversion Technology (phct), Dongguk University, Seoul 04620, Republic of Korea

[b] Department of Energy and Materials, Konkuk University, Chungju 27478, Republic of Korea

ARTICLE INFO

Keywords:
Aptasensor
Myoglobin
Boron nitride nanosheets
Au nanoparticles
High sensitivity

ABSTRACT

A novel electrochemical aptasensor based on gold nanoparticles decorated on boron nitride nanosheets (AuNPs/BNNSs) for the sensitive and selective detection of myoglobin (Mb) is reported. BNNSs were chemically synthesized by a low-cost and simple hydrothermal method. They were deposited onto the fluorine-doped tin oxide (FTO) electrode by a spin-coating method. Subsequently, AuNPs were chemically deposited onto the BNNS/FTO electrode by a seed-mediated chemical reduction method, with an average particle size of approximately 10 nm. The AuNPs/BNNSs/FTO electrode was used as a transducer to immobilize a thiol-functionalized DNA aptamer (Apt) via the covalent interaction of Au–S for the specific binding of Mb. $[Fe(CN)_6]^{3-/4-}$ was used as a redox probe to monitor the oxidation current variation upon the binding of Mb with varying concentrations onto the sensor surface. The Apt/AuNPs/BNNSs/FTO sensor shows a high signal response for Mb with a detection limit of 34.6 ng/mL and a dynamic response range of 0.1–100 μg/mL. It is a promising candidate for point-of-care diagnosis in real samples. This strategy could make possible the application of other 2D materials with wide bandgaps for the development of biosensors.

1. Introduction

The World Health Organization (WHO) indexed cardiovascular diseases (CVDs), such as coronary artery disease (CAD), heart failure, and hypertensive heart diseases, as the leading cause of death in developing and developed countries. An estimated 41.80% of CVD-affected people worldwide died in 2015 because of CAD, which includes angina and acute myocardial infarction (AMI). The leading cause of death for CAD-affected people is AMI, and the age-/sex-adjusted incidence rate of AMI is more than 200 cases per person-year (O'Gara et al., 2013). Thus, rapid and accurate diagnosis and prognosis of AMI have attracted great interest. According to the WHO guideline, AMI can be diagnosed by considering the following three symptoms: characteristic chest pain, changes in electrocardiography (ECG) reading, and elevation of cardiac biomarkers in biological fluids (Yang and Zhou, 2006; Tuteja et al., 2016). Although great success has been made in diagnosing AMI-suspected patients by ECG, a high percentage of AMI patients show nondiagnostic ECG or ambiguous readings (Pedrero et al., 2014). Thus, measuring the concentration of cardiac biomarkers in biological fluids is an effective method to diagnose AMI more accurately. Several potential cardiac biomarkers, including myoglobin (Mb), troponin I (TnI), C-reactive protein (C-RP), and creatine kinase-MB (CK-MB), have attracted the interest of researchers (Nowatzke et al., 2003). In particular, Mb plays an important role in the earlier diagnosis of AMI using blood serum samples. The normal concentration of Mb in biological fluid is in the range 0.48–0.90 nM (Zhang et al., 2016) or 100–200 ng/mL (Suprun et al., 2010). Mb is quickly released into the body's circulation within 4–5 h after AMI onset, and its concentration is elevated to ~4.8 μM (Wu et al., 1994). Thus, the development of a rapid, accurate, and sensitive detection method of Mb in body fluids is important.

The electrochemical method is well-suited to the rapid and sensitive detection of Mb compared with conventional expensive and time-consuming techniques, such as mass spectrometry, surface plasmon resonance, and the colorimetric method (Loo et al., 1989; Wang et al., 2015; Osman et al., 2013). Additionally, the electrochemical method has the advantages of short reading time, miniaturization ability, and low cost, and it requires a small amount of sample (Rahman et al., 2018, 2014a, 2014b, 2015). Numerous studies have been reported for the electrochemical detection of Mb using antibodies (Prakash et al., 2017; Billah et al., 2008). These antibody-based sensors have the limitations of low stability, high cost, and difficulty of chemical

* Corresponding authors.
E-mail addresses: mahbub1982@kku.ac.kr (Md. M. Rahman), jjlee@dongguk.edu (J.-J. Lee).

https://doi.org/10.1016/j.bios.2018.10.060
Received 15 September 2018; Received in revised form 25 October 2018; Accepted 27 October 2018
Available online 29 October 2018
0956-5663/

modification for biomolecule detection (Jo et al., 2015). Recently, aptamers (peptide molecules or sequences of oligonucleotide) have been developed as an alternative to antibodies with high specificity and selectivity, which can overcome the limitations of antibodies (Jo et al., 2015; Min et al., 2008; Maehashi et al., 2007; Medley et al., 2008). The aptamer is highly suitable for developing electrochemical sensors because of its ability to form a unique three-dimensional structure to capture the target biomolecules (Min et al., 2008). Additionally, the simple and easy chemical functionalization of aptamers makes their easy immobilization on the electrode surfaces possible. The modification of conventional electrode surfaces with functionalized nanomaterials, nanocomposites, and nanohybrids with high surface area is crucial to maximizing the number of aptamers immobilization. This can enhance the sensitivity of Mb detection and decrease the limit of detection. A number of electrode modifiers, including Au nanoparticles/arginine-glycine-aspartic acid/carboxylated graphene (Li et al., 2017), porphyrin functionalized graphene-conjugated gold nanoparticles (Zhang et al., 2016), and graphene-carbon nanotube nanohybrids (Kumar et al., 2015), were reported to enhance the sensitivity and to obtain a low detection limit for the electrochemical detection of Mb.

The application of various two-dimensional (2D) layered materials, such as boron nitride (BN), MoS_2, and graphitic carbon nitride, in addition to graphene, is highly advantageous for developing a nanoscale electrochemical sensing platform (Thanh et al., 2016). In particular, boron nitride nanosheets (BNNSs), composed of sp^2 bonded boron and nitrogen atoms, are of special interest because of their high surface area and easy functionalization (Singhal et al., 2013). The structure of BNNSs is similar to that of graphene, with carbons being replaced by boron and nitrogen (Deepak et al., 2002; Hattori et al., 2015), and it is easier to functionalize BNNSs by anchoring metal nanoparticles, such as AuNPs (Boukhvalov and Katsnelson, 2008). Although BNNSs are reliable insulators, some recent investigations have revealed that the functionalized form of BNNSs, such as AuNPs, polyamide-BN nanocomposites, and platinum-nanoparticle-loaded BN aerogel, can exhibit excellent catalytic activities for various electrochemical processes (Yang et al., 2014; Khan et al., 2016; Li et al., 2016; Aksoy et al., 2016).

In this work, an easy chemical strategy to prepare Au nanoparticle deposition on the surface of BNNSs (AuNPs/BNNSs) to develop a novel label-free aptasensor for Mb detection is presented for the first time (Scheme 1). BNNSs, being prepared from pristine BN powder by a simple hydrothermal method at room temperature, were used as a nanoscale platform for the deposition of AuNPs. A homogeneous distribution of AuNPs over BNNSs provides a large-area excellent catalytic matrix to maximize aptamer immobilization for sensitivity enhancement.

2. Materials and methods

2.1. Materials

Mb, BN powder, sulfuric acid (98%), $KMnO_4$, H_2O_2, gold chloride hydrate, tris[2-carboxyethyl] phosphine) (TECP), human serum, ascorbic acid (AA), glucose oxidase, sarcosine oxidase, sodium dihydrogen phosphate (NaH_2PO_4), disodium hydrogen phosphate (Na_2HPO_4), and insulin from porcine pancreas were purchased from Sigma-Aldrich (St. Louis, Missouri, USA). Fluorine-doped tin oxide (FTO)-coated glass substrates with a sheet resistance of 8 Ω/sq. were purchased from Pilkington (USA). DNA aptamers with disulfide functionalization (C6 S-S) at the 5′ end with a sequence of 5′-CCCTCCTTT CCTTCGACGTAGATCTGCTGCGTTGTTCCGA-3′ for target-specific Mb binding (Li et al., 2017) were purchased from Cosmo Genetech Co. Ltd (Seoul, Korea). A phosphate buffer solution (PB) with a pH of 7.0 was prepared according to a previously reported procedure (Rahman et al., 2014a, 2014b).

2.2. Synthesis of BNNSs and the preparation of BNNSs/FTO electrode

The hexagonal BNNSs were synthesized according to a previously reported method (Du et al., 2013). Briefly, 2 g of pristine BN powder was added into H_2SO_4 (98%, 50 mL) solution and stirred for 30 min. Then, $KMnO_4$ (1 g) was added slowly to the mixture at 0 °C and stirred for 12 h. Subsequently, H_2O_2 (30% w/w, 5 mL) was added to the mixture and stirred again for another 5 h. The resulting suspension was centrifuged at 3000 rpm for 10 min to remove the larger BN particles. Then, the supernatant was sequentially centrifuged and washed with water until the solution pH reached 7.0. Finally, the supernatant was filtered to obtain BNNSs, which were dried in a vacuum oven at 40 °C for 24 h.

Prior to the preparation of the BNNSs/FTO electrode (2 cm × 2 cm), the FTO (TEC-8, Pilkington, USA) was cleaned sequentially with water and ethanol by sonication and dried by N_2 gas. A BNNS paste was prepared by mixing BNNSs with terpineol solution (~95%), which was deposited on FTO by a spin-coating method. Then, the electrode was heat treated at 200 °C for 12 h to remove the terpineol binder. The average thickness of the BNNS film was approximately 300 ± 5 nm.

2.3. Deposition of AuNPs on BNNSs/FTO

A simple chemical reduction method was used to prepare the AuNPs onto the BNNSs/FTO electrode (Thanh et al., 2016). The BNNSs/FTO was dipped into $HAuCl_4$ (0.5 mM) in PB (pH 7.0) for 1 h at 70 °C. This allowed the adsorption of Au^{3+} onto the BNNS surface by covalent interaction with N (Radenković et al., 2017). Then, the electrode was removed from the solution and washed with water to remove the unbound Au^{3+}. Subsequently, the electrode was dipped into an AA solution (1 mM) for 1 h to reduce Au^{3+} to Au^0 (Thanh et al., 2016). The

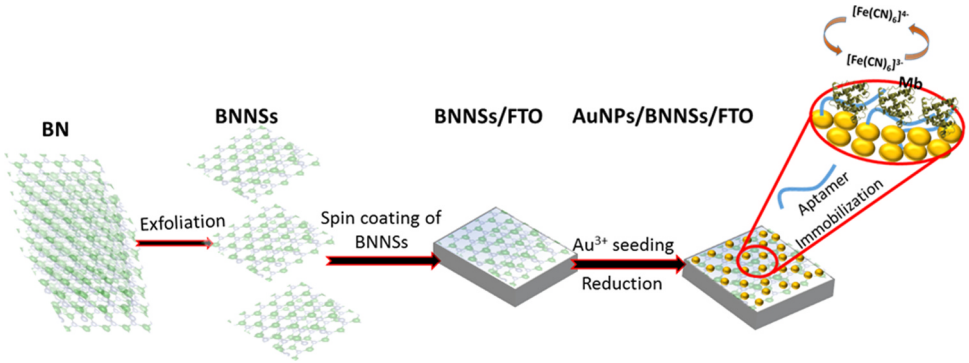

Scheme 1. Schematic illustration for the fabrication processes of the aptasensor and the detection of Mb.

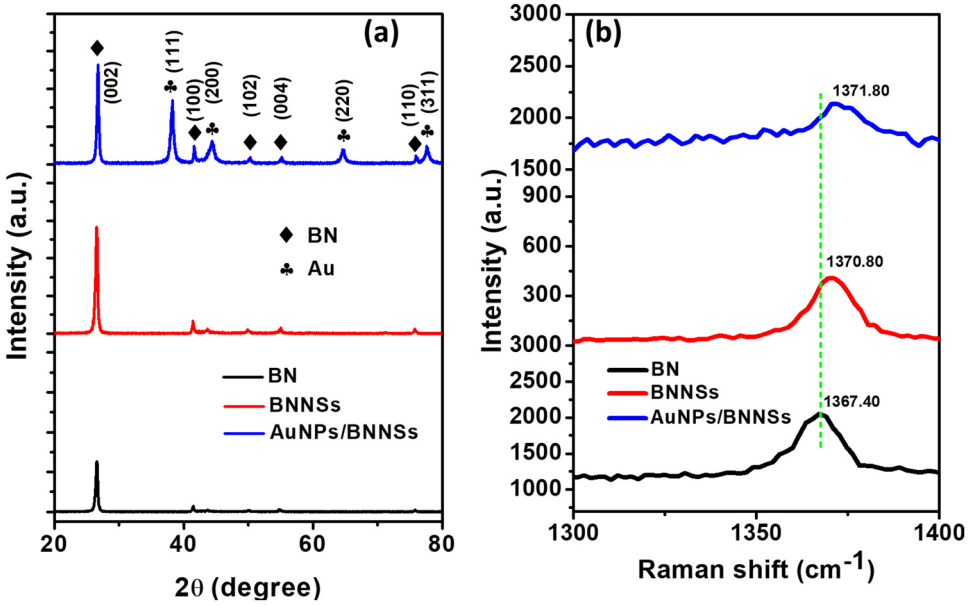

Fig. 1. (a) XRD pattern and (b) Raman spectra of pristine BN, BNNSs, and AuNPs/BNNSs.

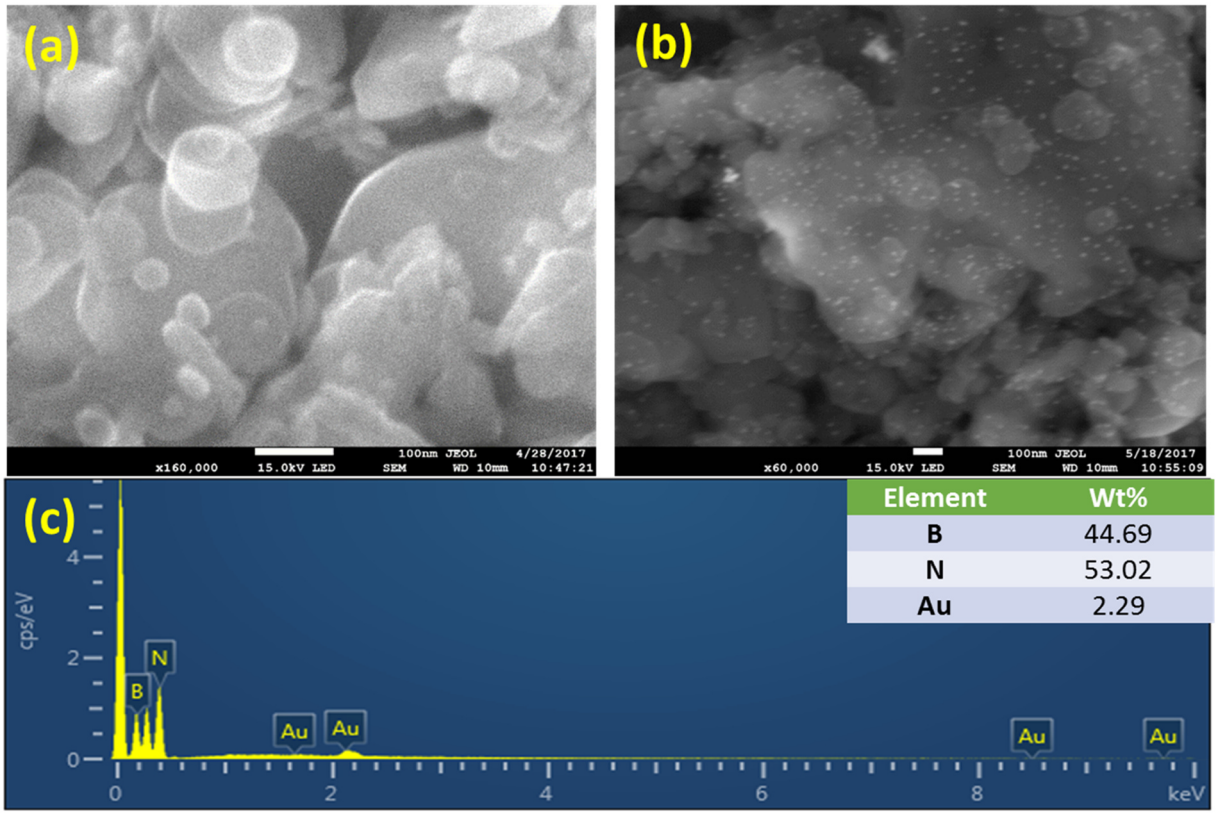

Fig. 2. FE-SEM image of (a) as-prepared BNNSs and (b) AuNPs/BNNSs/FTO electrode. (c) the EDS spectrum of AuNPs/BNNSs/FTO (inset shows the elemental compositions).

obtained AuNPs/BNNSs/FTO electrode was washed with water and dried by N_2 gas.

2.4. Immobilization of aptamer

Prior to the immobilization of aptamers, disulfide-functionalized aptamers were reduced using TCEP (Burns et al., 1991). Briefly, TCEP (100 μM) was added to the disulfide-functionalized aptamer solution (10 mL, 1 μM). Then, the mixture was kept at room temperature for 5 h, which reduced the disulfide-functionalized aptamer to thiol-functionalized aptamer. Subsequently, the AuNPs/BNNSs/FTO electrode was dipped into the reduced aptamer solution for 12 h at room temperature. This made possible the immobilization of aptamers on the AuNP surface via the covalent interaction of Au–S. The aptamer-modified AuNPs/BNNSs/FTO electrode (Apt/AuNPs/BNNSs/FTO) was washed with PB (pH 7.0) and dried. The Apt/AuNPs/BNNSs/FTO sensor was dipped

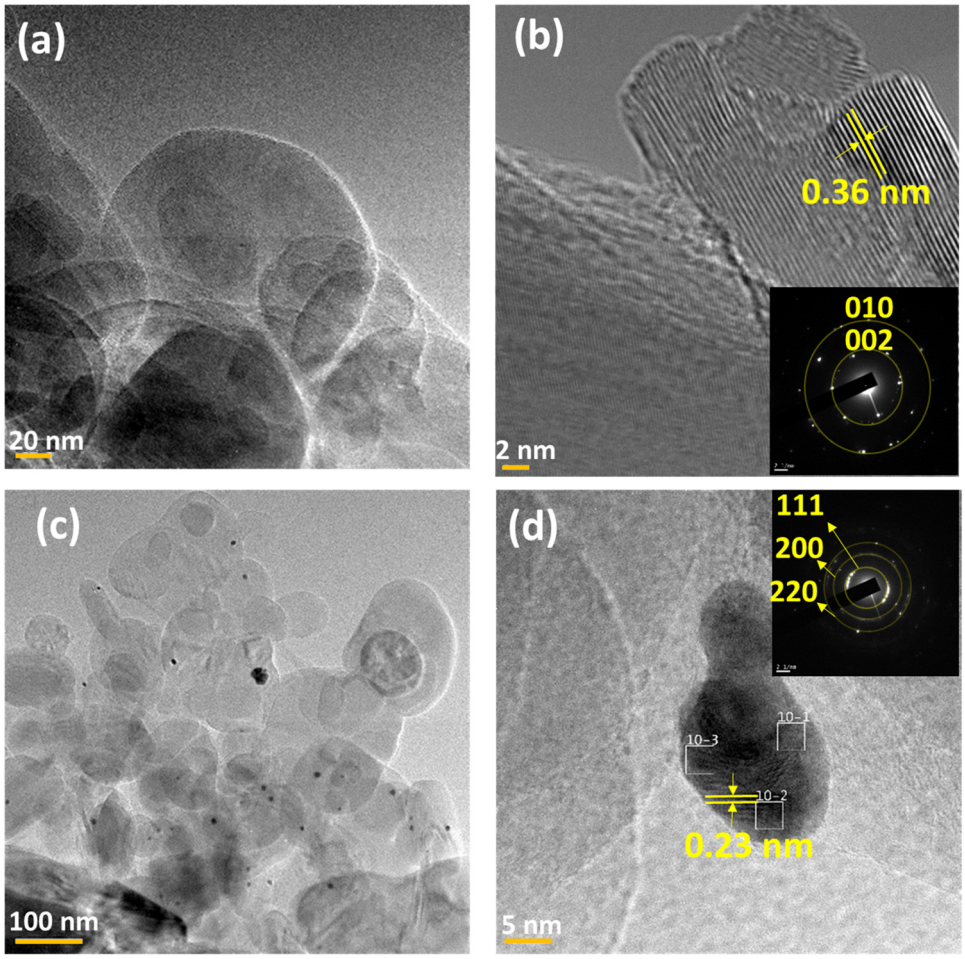

Fig. 3. HR-TEM images of (a) and (b) BNNSs (inset of (b) shows the SAED pattern of BNNSs) and (c) and (d) HR-TEM images of AuNPs/BNNSs and lattice fringes of AuNPs (inset of (d) shows the SAED pattern of AuNPs).

again into a solution of 2-mercaptoethanol (1 mM in ethanol) for another 5 h to prevent the nonspecific binding of the target Mb.

2.5. Instrumentation

The crystallographic phases of BN powder, BNNSs, and AuNP were analyzed by an X-ray diffractometer (XRD, D8 Advance, Bruker, Germany) with Cu K_α radiation of $\lambda = 1.5406$ Å, accelerating voltage of 40 kV, and a cathode current of 30 mA. The UV–visible absorption spectrum of the samples was analyzed by a UV–visible spectrophotometer (S-3100, SCINCO). Field emission scanning electron microscopy (FE-SEM, JEOL, JSM-6700F) was used to characterize the morphologies of the samples. Energy dispersive X-ray spectroscopy (EDS, INCAx-sight7421, Oxford Instruments), equipped with the FE-SEM instrument, was used to analyze the elemental composition of the samples. A high-resolution transmission electron microscopy (HR-TEM) was used to analyze the morphology and selected area diffraction pattern (SAED) of the samples. Raman spectroscopic (Horiba Scientific, Xplora Plus, France) measurement was performed at room temperature with an excitation wavelength of 532 nm. X-ray photoelectron spectra (XPS) were measured by an XPS analyzer (XPS, Thermo Scientific K-Alpha, Thermo Fisher Scientific, UK).

All the electrochemical measurements were performed at room temperature using an electrochemical workstation (CHI 430A, CH Instruments, Inc., USA). A conventional three-electrode system was used, where the bare FTO or modified FTO electrode served as a working electrode. Ag/AgCl and Pt wire were used as a reference and counter electrode, respectively. A differential pulse voltammogram (DPV) was attained with a pulse amplitude, pulse width, and pulse period of 100 mV s^{-1}, 2 ms, and 100 ms, respectively. Electrochemical impedance spectroscopy (EIS) was performed with an EIS analyzer (IM6ex, Zahner-Elektrik GmbH & Co. KG) in a frequency range of 0.1 Hz–1 MHz at + 0.3 V with an AC amplitude of 5 mV. The EIS parameter was obtained by fitting the EIS spectra using Z-view software (version 3.1, Scribner Associates Inc., USA).

3. Results and discussion

3.1. XRD and Raman analysis

X-ray diffraction (XRD) and Raman analysis were performed to investigate the crystallographic phase structures of BNNSs and AuNPs/BNNSs. Fig. 1(a) shows the XRD pattern of pristine BN, BNNSs, and AuNPs/BNNSs in the 2θ range of 20–80°. All the samples exhibited the characteristic XRD pattern of BN at approximately 26.70°, 41.65°, 50.32°, 55.0°, and 75.80° with the corresponding *hkl* reflections of (002), (100), (102), (004), and (110), respectively. This indicates that the pristine BN and BNNSs are of hexagonal phase (JCPDS card 34-0421) (Wang et al., 2009). The 2θ value of the (002) diffraction peak in the BNNSs was shifted to a lower angle by increasing the intensity compared with that of the pristine BN powder. The increased full width at half maximum (FWHM) of the (002) diffraction peak of BNNSs specifies the thickness reduction (i.e., the decrease in the number of layers) due to the exfoliation of BN powder (Kumari et al., 2015) (Fig. S1). This can be attributed to pristine BN being exfoliated mostly along the (002) plane. The XRD pattern of the AuNPs/BNNSs exhibited

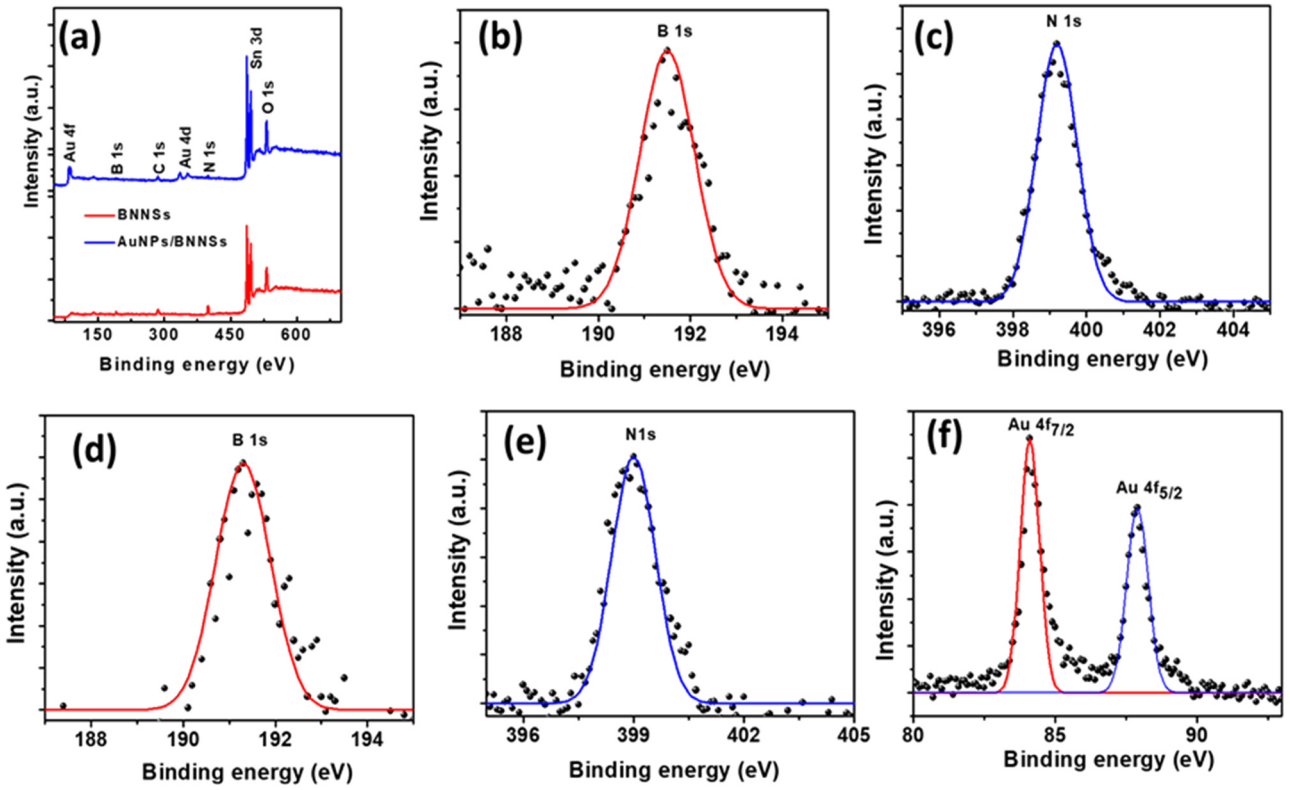

Fig. 4. (a) XPS survey spectra of BNNSs and AuNPs/BNNSs modified FTO electrodes, (b) and (c) narrow-scan XPS spectra of B 1s and N 1s in BNNSs, respectively, and (d) and (f) narrow-scan XPS spectra of B 1s, N 1s, and Au 4f in AuNPs/BNNSs, respectively (the dotted and solid lines designate the experimental and fitted data, respectively).

additional peaks at 2θ of approximately 38.3°, 44.4°, 64.6°, and 77.7° with the corresponding *hkl* reflections of (111), (200), (220), and (311), respectively. This specifies that AuNPs are of face-centered-cubic (fcc) phase (JCPDS card 4-784) (Wang et al., 2011). The intense peak at 2θ of approximately 38.3° represents the preferential growth of AuNPs along the (111) direction. These results confirmed the successful exfoliation of BNNSs and the deposition of AuNPs onto BNSSs with good crystallinity.

Fig. 1(b) shows the Raman spectra of pristine BN, BNNSs, and AuNPs/BNNSs. The characteristic Raman band of boron nitride was observed at approximately 1367.40, 1370.80, and 1371.80 cm^{-1}, respectively, for pristine BN, BNNSs, and AuNPs/BNNSs. This can be attributed to the E_{2g} vibration mode of hexagonal BN (Geick et al., 1966). The shifting of the Raman band to a higher frequency for BNNSs compared with the pristine BN with lowering the intensity indicates the successful exfoliation of pristine BN (Gorbachev et al., 2011), whereas the additional Raman band shift to a higher frequency for AuNPs/BNNSs than the BNNSs with lowered additional peak intensity could be caused by the deposition of AuNPs onto BNNSs.

3.2. Morphological analysis

Fig. 2 shows the FE-SEM images of BNNSs and AuNPs/BNNSs. Unlike the random aggregation of the pristine BN powder (Fig. S2), BNNSs clearly showed good stacking of the exfoliated sheets with less aggregation. The FE-SEM image of AuNPs/BNNSs indicates the uniform distribution of AuNPs with an average particle size of ~10 nm. The EDS elemental mapping of AuNPs/BNNSs, shown in Fig. 2(c), supports the stable formation of AuNPs on BNNSs. Fig. 3 shows the HR-TEM images and the SAED pattern of the BNNSs and AuNPs/BNNSs. The BNNSs showed good transparency to an electron beam, because of the small number of sheets present in the BNNSs. The spacing between the adjacent fringes is approximately 0.36 nm, which is close to the calculated *d* spacing from the XRD data for the (002) diffraction plane, and it is consistent with the reported value (Lin et al., 2016). The SAED pattern exhibits the bright spots of (002) and (010) planes. These specifics indicate that the BNNSs are of hexagonal structure with high crystallinity, and this is consistent with the XRD results. In contrast, the HR-TEM images of AuNPs/BNNSs clearly reveal the successful deposition of AuNPs in the BNNSs. The interplanar spacing between the adjacent fringes of Au is approximately 0.23 nm, which is close to the calculated *d* spacing from the XRD data for the (111) diffraction plane (Macdonald et al., 2016). The SAED pattern of the AuNPs shows the bright rings of (111), (200), and (220) planes, indicating the high crystallinity of AuNPs.

3.3. XPS and UV–visible spectroscopic analysis

XPS is a powerful and sensitive tool to investigate the elemental stoichiometry in the samples. Fig. 4(a) shows the XPS survey spectra of BNNSs and AuNPs/BNNSs. Both spectra clearly reveal the presence of B 1s and N 1s peaks arising from BNNSs. AuNPs/BNNSs show an additional peak of Au 4f, indicating the successful incorporation of AuNPs into BNNSs. The narrow scan spectra of B 1s and N 1s in BNNSs, as shown in Fig. 4(b) and (c), peak at approximately 191.50 and 399.20 eV, respectively, which is in good agreement with the previously reported values (Wang et al., 2011; Jalaly et al., 2017). However, in AuNPs/BNNSs, these peaks were positioned at approximately 191.30 and 399 eV, respectively, as seen in Fig. 4(d) and (e). The negligible peak shifting and unaltered peak intensity indicate that the chemical oxidation state and composition of BNNSs were unchanged upon the deposition of AuNPs. The core-level Au 4f spectrum of AuNPs/BNNSs exhibits two main peaks of Au $4f_{7/2}$ and Au $4f_{5/2}$ at binding energies of approximately 84.10 and 87.85 eV, respectively, as in Fig. 4(f). The binding energy of these two peaks is close to the binding energy of metallic Au (Joseph et al., 2003). These findings support the

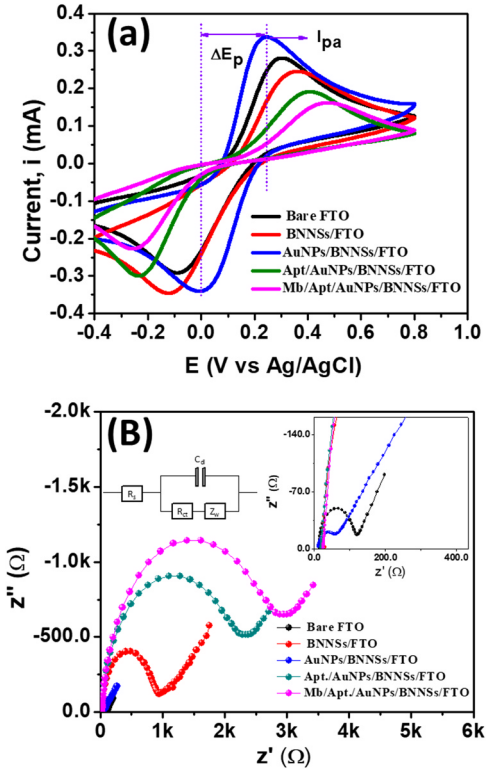

Fig. 5. (a) CVs of electrodes in $[Fe(CN)_6]^{3-/4-}$ (5 mM each) in PB (pH 7.0) at a scan rate of 100 mV/s and (b) EIS spectra of the corresponding electrodes in $[Fe(CN)_6]^{3-/4-}$ (5 mM each) in PB (pH 7.0) (upper inset of (b) shows the magnified spectra at the high-frequency region, while the lower Inset shows the Randles equivalent circuit model to fit the EIS spectra; the Mb concentration was 100 μg/mL).

existence of the interaction of AuNPs with BNNSs.

Additionally, the UV–vis spectrum of BNNS dispersion in ethanol and AuNPs/BNNSs/FTO electrode was also measured. The BNNSs exhibit an absorption maximum (λ_{max}) at 200 nm, which is consistent with previous reports (Ba et al., 2016) (Fig. S3). No other additional absorption band was observed, which indicates the high purity of the BNNSs. The AuNPs/BNNSs/FTO electrode, however, showed a characteristic absorption band of AuNPs at λ_{max} of 500 nm (Fig. S4) (Zuber et al., 2016).

3.4. Electrochemical characterization

Fig. 5(a) and (b) show the cyclic voltammograms (CVs) and EIS spectra of electrodes in a solution of $[Fe(CN)_6]^{3-/4-}$ (5 mM each in PB). The anodic peak current (I_{pa}) for the oxidation of $[Fe(CN)_6]^{3-}$ at bare FTO was approximately 0.28 mA, with a peak potential separation (ΔE_p) of about 0.38 V. These values were approximately 0.24 mA and 0.46 V for BNNS/FTO and ~0.34 mA and ~0.32 V for AuNPs/BNNSs/FTO. The initial decrease in the electrocatalytic property for BNNSs/FTO is attributable to the insulating nature of BNNSs (Khan et al., 2016), while it was compensated for by the highly catalytic AuNPs deposited on the BNNS (AuNPs/BNNSs/FTO). The values of I_{pa} and ΔE_p were ~0.19 ± 0.002 mA and ~0.50 V upon immobilization of aptamers for Apt/AuNPs/BNNSs/FTO, and they became ~0.16 ± 0.005 mA and ~0.70 V at Mb/Apt/AuNPs/BNNSs/FTO, after the attachment of Mb onto the aptamers. The continuous decrease in the electrocatalytic property over the redox reaction of $[Fe(CN)_6]^{3-/4-}$, by decreasing the peak current and widening of the voltammogram, is attributable to the increase of electrostatic repulsion between the negatively charged $[Fe(CN)_6]^{3-/4-}$ with the negatively charged PO_4^{3-} groups of aptamer (Rahman et al., 2015, 2016). Similarly, the non-conducting properties of Mb further hampered the electron transport (Li et al., 2017). The variations of I_{pa} and ΔE_p upon consecutive surface modification were consistent with the variation of the interfacial charge

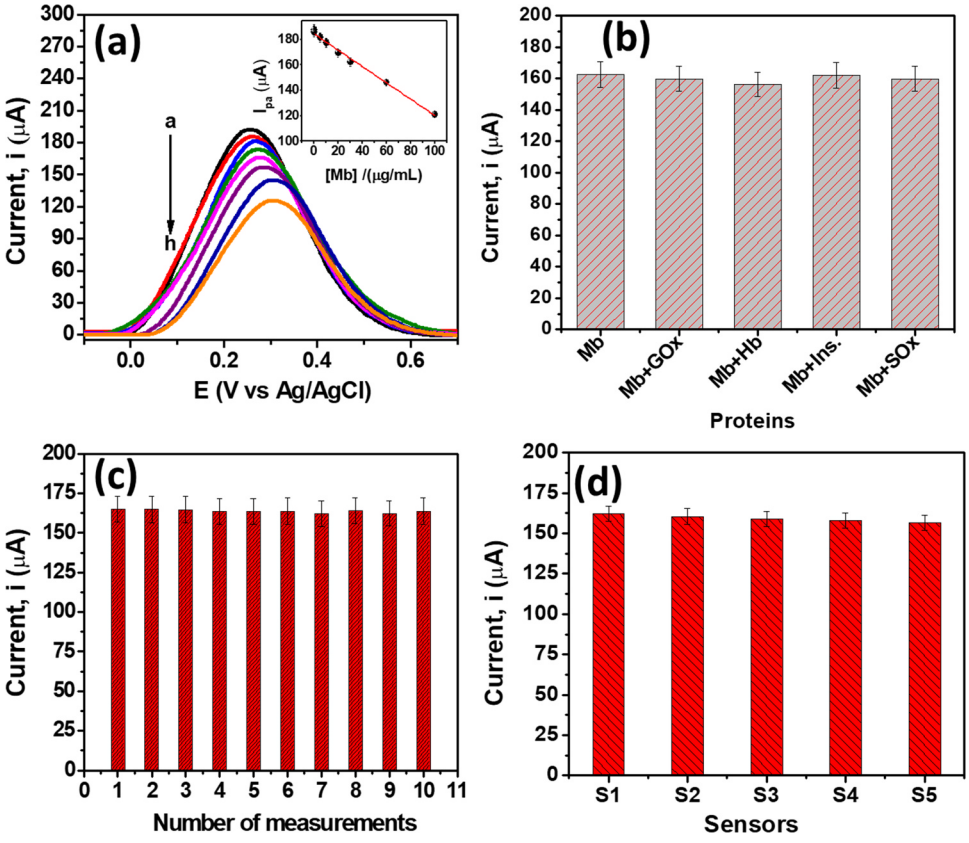

Fig. 6. (a) DPV responses of $[Fe(CN)_6]^{3-/4-}$ oxidation at different concentrations (a→h: (0, 0.1, 5, 10, 20, 30, 60, and 100 μg/mL) of target Mb-attached Apt/AuNP/BNNS/FTO sensor (inset shows the plot of I_{pa} vs. Mb concentration), variation of the I_{pa} of $[Fe(CN)_6]^{3-/4-}$ oxidation at the Mb-attached (30 μg/mL) aptasensor, (b) without and with the presence of interferences, (c) consecutive DPV measurements, and (d) five independent sensors; the error bars indicate the percentage error range (5%).

transfer resistance (R_{ct}) obtained from the EIS spectra, which were approximately 104, 900, 48, 2250, and 2900 Ω at bare FTO, BNNSs/FTO, AuNPs/BNNSs/FTO, Apt/AuNPs/BNNSs/FTO, and Mb/Apt/AuNPs/BNNSs/FTO, respectively.

Fig. S5 shows the CVs of BNNSs/FTO and AuNPs/BNNSs/FTO electrodes in PB solution (pH 7.0), which clearly indicate the formation of the AuNP layer on BNNSs/FTO by showing the formation of gold oxide on the AuNPs (Rahman et al., 2014a, 2014b), peaking at approximately 0.72 V by positive polarization, and then reducing to approximately 0.27 V during the reverse scan, while there was no redox signal for BNNSs/FTO.

3.5. Detection of Mb and interference studies

The Apt/AuNPs/BNNSs/FTO sensor was incubated in varying concentrations of target Mb in PB (pH 7.0) before the DPV measurements. Fig. 6(a) shows the DPV responses of $[Fe(CN)_6]^{3-/4-}$ oxidation after the attachment of Mb on an Apt/AuNPs/BNNSs/FTO sensor with varying concentrations. The results demonstrate that the I_{pa} of $[Fe(CN)_6]^{3-/4-}$ decreased with the increase of the concentration of the target Mb. A linear relationship was observed between the I_{pa} of $[Fe(CN)_6]^{3-/4-}$ and the concentration of Mb, with a linear regression equation of I_{pa} (μA) = 184.70–0.641 [Mb](μg/mL) (R^2 = 0.993). This corresponds to the detection limit and sensitivity of 34.6 ng/mL and 0.641 μA/μg/mL, respectively. Although the detection limit of this sensor is lower than those of some other reported aptasensors for the detection of Mb (Table S1), it is suitable for the detection of Mb in biological fluids within the normal concentration range.

The selectivity of the proposed electrochemical aptasensor was investigated using some possible interfering proteins, including hemoglobin (Hb), glucose oxidase (GO_x), insulin (Ins.), and sarcosine oxidase (SO_x). The concentration of these interfering proteins was five times higher than the concentration of Mb (30 μg/mL). Fig. 6(b) shows the variation of the I_{pa} of $[Fe(CN)_6]^{3-/4-}$ at the Mb-attached Apt/AuNPs/BNNSs/FTO sensor in the presence and absence of interferences. This indicates that the interfering proteins do not alter the I_{pa} of $[Fe(CN)_6]^{3-/4-}$ significantly after incubating the Apt/AuNPs/BNNSs/FTO sensor in the mixed solution of Mb and other proteins. The maximum I_{pa} decreased only approximately 4% in the presence of Hb. This specifies the high specificity and selectivity of the sensor for the detection of Mb.

3.6. Stability, reproducibility, and real-sample analyses

The electrochemical stability of the sensor was tested by consecutive DPV measurements (10 times) of $[Fe(CN)_6]^{3-/4-}$ oxidation using a Mb (30 μg/mL) attached Apt/AuNPs/BNNSs/FTO sensor without any treatment in between the DPV measurements. The variation of I_{pa} was significantly low with a relative standard deviation (RSD) of only 0.50% (Fig. 6c). Additionally, it was observed that the sensor retained approximately 93.68% of its initial response after being stored in PB (pH 7.0) at 4 °C for 30 days. This indicates the high storage stability of this sensor. The reproducibility of the sensor was verified by DPV measurement of $[Fe(CN)_6]^{3-/4-}$ at five independent Mb (30 μg/mL) attached sensors, which showed that the RSD of I_{pa} was only 1% (Fig. 6d).

PB (pH 7.0) diluted (100 times) human serum (Sigma-Aldrich) samples were used as real samples to investigate the practical applicability of the sensor. This was tested by incubating the sensor in real samples containing (30 and 60) μg/mL of Mb. After the attachment of Mb, the DPV responses were measured, and the I_{pa} was compared with an external calibration plot. The average relative recoveries for (30 and 60 μg/mL of Mb were 104.39% and 102.48%, respectively. These results indicate that the proposed aptasensor can detect Mb in real biological samples with high accuracy, and it is promising for physiological and pathological studies.

4. Conclusion

Gold nanoparticles deposited on boron nitride nanosheets (AuNPs/BNNSs) for the aptamer-based electrochemical sensing of Mb were developed with high stability and reproducibility. $[Fe(CN)_6]^{3-/4-}$ was used as a redox probe to monitor the variation of its oxidation signal as a function of the concentration of Mb. The N atoms in the two-dimensional BNNSs facilitated the deposition of AuNPs, which offered a large-surface-area platform of the effective immobilization of thiol-functionalized aptamers. The specific binding of Mb on this aptamer layer induced a decrease of the electrochemical catalytic properties of the Apt/AuNPs/BNNSs/FTO electrode surface. This aptasensor showed a significantly low value of detection limit (S/N = 3, 34.6 ng/mL) with relatively high sensitivity (0.641 μA/μg/mL) over a wide linear range (0.1–100 μg/mL). This can be applicable to the development of a Suprun novel and promising platform for the early accurate screening and diagnosis of AMI in clinical applications.

Acknowledgments

This research was supported by the Basic Science Research Program through the National Research Foundation of Korea (NRF), funded by the Ministry of Education (2015R1D1A1A01057380, NRF-2016R1A2B2012061). This work was also partly supported by the Dongguk University Student Research Development Fund (SRD − 1) of 2016.

Appendix A. Supporting information

Supplementary data associated with this article can be found in the online version at doi:10.1016/j.bios.2018.10.060

References

Aksoy, B., Paşahan, A., Güngör, Ö., Köytepe, S., Seçkin, T., 2016. Int. J. Polym. Mater. Polym. Biomater. 66, 203–212.
Ba, K., Jiang, W., Cheng, J., Bao, J., Xuan, N., Sun, Y., Liu, B., Xie, A., Wu, S., Sun, Z., 2016. Sci. Rep. 7, 45584.
Billah, M., Hays, H.C.W., Millner, P.A., 2008. Microchim. Acta 160, 447–454.
Boukhvalov, D.W., Katsnelson, M.I., 2008. Phys. Rev. B 78, 085413.
Burns, J.A., Butler, J.C., Moran, J., Whitesides, G.M., 1991. J. Org. Chem. 56, 2648–2650.
Du, M., Wu, Y., Hao, X., 2013. CrystEngComm 15, 1782–1786.
Deepak, F., Vinod, C., Mukhopadhyay, K., Govindaraj, A., Rao, C.N., 2002. Chem. Phys. Lett. 353, 345–352.
Gorbachev, R.V., Riaz, I., Nair, R.R., Jalil, R., Britnell, L., Belle, B.D., Hill, E.W., Noveselov, E.S., Watanabe, K., Taniguchi, T., 2011. Small 7, 465–468.
Geick, R., Perry, C.H., Rupprecht, G., 1966. Phys. Rev. 146, 543.
Hattori, Y., Taniguchi, T., Watanabe, K., Nagashio, K., 2015. ACS Nano 9, 916–921.
Jalaly, M., Gotor, F.J., Semnan, M., Sayagués, M.J., 2017. Sci. Rep. 7, 3453.
Jo, H., Gu, H., Jeon, W., Youn, H., Her, J., Kim, S.-K., Lee, J., Shin, J.H., Ban, C., 2015. Anal. Chem. 87, 9869–9875.
Joseph, Y., Besnard, I., Rosenberger, M., Guse, B., Nothofer, H.-G., Wessels, J.M., Wild, U., Knop-Gericke, A., Su, D., Schlögl, R., Yasuda, A., Vossmeyer, T., 2003. J. Phys. Chem. B 107, 7406–7413.
Khan, A.F., Brownson, D.A.C., Randviir, E.P., Smith, G.C., Banks, C.E., 2016. Anal. Chem. 88, 9729–9737.
Kumar, V., Shorie, M., Ganguli, A.K., Sabherwal, P., 2015. Biosens. Bioelectron. 72, 56–60.
Kumari, S., Sharma, O.P., Gusain, R., Mungse, H.P., Kukrety, A., Kumar, N., Sagimura, H., Khatri, O.P., 2015. ACS Appl. Mater. Interfaces 7, 3708–3716.
Li, C., Li, L., Yang, X., Gao, L., Jing, L., Ma, X., 2017. Sens. Actuators B-Chem. 242, 1239–1245.
Li, Q., Luo, W., Su, L., Chen, J., Chou, K.-C., Hou, X., 2016. RSC Adv. 6, 92748–92753.
Lin, L., Liu, T., Zhang, Y., Sun, R., Zeng, W., Wang, Z., 2016. Ceram. Int. 42, 971–975.
Loo, J.A., Udseth, H.R., Smith, R.D., 1989. Anal. Biochem. 179, 404–412.
Macdonald, T.J., Wu, K., Sehmi, S.K., Noimark, S., Peveler, W.J., du Toit, H., Voelcker, N.H., Allan, E., MacRobert, A.J., Gavriilidis, A., Parkin, I.P., 2016. Sci. Rep. 6, 39272.
Medley, C.D., Smith, J.E., Tang, Z., Wu, Y., Bamrungsap, S., Tan, W., 2008. Anal. Chem. 80, 1067–1072.
Min, K., Cho, M., Han, S.Y., Shim, Y.B., Ku, J., Ban, C., 2008. Biosens. Bioelectron. 23, 1819–1824.
Maehashi, K., Katsura, T., Kerman, K., Takamura, Y., Matsumoto, K., Tamiya, E., 2007. Anal. Chem. 79, 782–787.
Nowatzke, W.L., Cole, T.G., Chambless, L.E., Lemos, J.A., de, Virani, S.S., Agarwal, S., Boerwinkle, E., Hoogeveen, R.C., Aguilar, D., Astor, B.C., Srinivas, P.R., Deswal, A.,

Mosley, T.H., Coresh, J., Folsom, A.R., Heiss, G., Ballantyne, C.M., 2003. Clin. Chem. 49, 1560–1562.
O'Gara, P.T., Kushner, F.G., Ascheim, D.D., Casey Jr., D.E., Chung, M.K., de Lemos, J.A., Ettinger, S.M., Fang, J.C., Fesmire, F.M., Franklin, B.A., Granger, C.B., Krumholz, H.M., Linderbaum, J.A., Morrow, D.A., Newby, L.K., Ornato, J.P., Ou, N., Radford, M.J., Tamis-Holland, J.E., Tommaso, C.L., Tracy, C.M., Woo, Y.J., Zhao, D.X., Anderson, J.L., Jacobs, A.K., Halperin, J.L., Albert, N.M., Brindis, R.G., Creager, M.A., DeMets, D., Guyton, R.A., Hochman, J.S., Kovacs, R.J., Kushner, F.G., Ohman, E.M., Stevenson, W.G., Yancy, C.W., 2013. Circulation 127, e362–e425.
Osman, B., Uzun, L., Beşirli, N., Denizli, A., 2013. Mater. Sci. Eng. C 33, 3609–3614.
Prakash, M.D., Singh, S.G., Sharma, C.S., Krishna, V.S.R., 2017. Electroanalysis 29, 380–386.
Pedrero, M., Campuzano, S., Pingarrón, J.M., 2014. Electroanalysis 26, 1132–1153.
Rahman, M.M., Ahmed, A., Lee, J.-J., 2018. J. Electrochem. Soc. 165, B89–B95.
Radenković, S., Antić, M., Savić, N.D., Glišić, B.Đ., 2017. New J. Chem. 41, 12407–12415.
Rahman, M.M., Lopa, N.S., Kim, Y.J., Choi, D.-K., Lee, J.-J., 2016. J. Electrochem. Soc. 163, B153–B157.
Rahman, M.M., Kim, Y.J., Lee, J.-J., 2015. J. Electrochem. Soc. 162, B159–B162.
Rahman, M.M., Li, X.-B., Kim, J., Lim, B.O., Ahammad, A.J.S., Lee, J.-J., 2014a. Sens. Actuators B-Chem. 202, 536–542.
Rahman, M.M., Li, X.-B., Lopa, N.S., Lee, J.-J., 2014b. Korean Chem. Soc. 35, 2072–2076.
Singhal, S.K., Kumar, V., Stalin, K., Choudhary, A., Teotia, S., Reddy, G.B., Mathur, R.B., Singh, S.P., Pasricha, R., 2013. Part. Syst. Charact. 30, 445–452.
Suprun, E., Bulko, T., Lisitsa, A., Gnedenko, O., Ivanov, A., Shumyantseva, V., Archakov, A., 2010. Biosens. Bioelectron. 25, 1694–1698.
Thanh, T.D., Balamurugan, J., Lee, S.H., Kim, N.H., Lee, J.H., 2016. Biosens. Bioelectron. 81, 259–267.
Tuteja, S.K., Chen, R., Kukkar, M., Song, C.K., Mutreja, R., Singh, S., Paul, A.K., Lee, H., Kim, K.-H., Deep, A., Suri, C.R., 2016. Biosens. Bioelectron. 86, 548–556.
Wang, Q., Yang, X., Yang, X., Liu, F., Wang, K., 2015. Sens. Actuators B-Chem. 212, 440–445.
Wang, Z., Zhao, S., Zhu, S., Sun, Y., Fang, M., 2011. CrystEngComm 13, 2262–2267.
Wang, L., Xu, L., Sun, C., Qian, Y., 2009. J. Mater. Chem. 19, 1989–1994.
Wu, A.H.B., Laios, I., Green, S., Gornet, T.G., Wong, S.S., Parmley, L., Tonnesen, A.S., Plaisier, B., Orlando, R., 1994. Clin. Chem. 40, 796–802.
Yang, G.-H., Abulizi, A., Zhu, J.-J., 2014. Ultrason. Sonochem. 21, 1958–1963.
Yang, Z., Zhou, D.M., 2006. Clin. Biochem. 39, 771–780.
Zhang, G., Liu, Z., Wang, L., Guo, Y., 2016. Sensors 16, 1803.
Zuber, A., Purdey, M., Schartner, E., Forbes, C., van der Hoek, B., Giles, D., Abell, A., Monro, T., Ebendorff-Heidepriem, H., 2016. Sens. Actuators B-Chem. 227, 117–127.